# Comparative Spectral Analysis of the Superluminous Supernova 2019neq

Réka Könyves-Tóth<sup>1,2</sup>, Benjamin P. Thomas<sup>3</sup>, József Vinkó<sup>1,2,3,4</sup>, and J. Craig Wheeler<sup>3</sup>, Konkoly Observatory, CSFK, Konkoly-Thege M. ut 15–17, Budapest, 1121, Hungary; konyvestoth.reka@csfk.mta.hu

<sup>2</sup> ELTE Eötvös Loránd University, Institute of Physics, Pázmany Péter sétány 1/A, Budapest, 1117, Hungary

<sup>3</sup> Department of Astronomy, University of Texas at Austin, 2515 Speedway, Stop C1400 Austin, TX 78712-1205, USA

<sup>4</sup> Department of Optics and Quantum Electronics, University of Szeged, Dóm tér 9, Szeged, 6720, Hungary

\*\*Received 2020 April 1; revised 2020 July 16; accepted 2020 July 23; published 2020 September 2

#### **Abstract**

We present a spectroscopic analysis of the recently discovered fast-evolving Type I superluminous supernova (SLSN-I) SN 2019neq (at redshift z = 0.1059). We compare it to the well-studied slowly evolving SLSN-I SN 2010kd (z = 0.101). Our main goal is to search for spectroscopic differences between the two groups of SLSNe-I. Differences in the spectra may reveal different ejecta compositions and explosion mechanisms. Our investigation concentrates on optical spectra observed with the 10 m Hobby-Eberly Telescope Low Resolution Spectrograph-2 at McDonald Observatory during the photospheric phase. We apply the SYN++ code to model the spectra of SN 2019neq taken at -4 days, +5 days, and +29 days from maximum light. We examine the chemical evolution and ejecta composition of the SLSN by identifying the elements and ionization states in its spectra. We find that a spectral model consisting of O III, Co III, and Si IV gives a SYN++ fit that is comparable to the typical SLSN-I spectral model consisting of O II, and conclude that the true identification of those lines, at least in the case of SN 2019neq, is ambiguous. Based on modeling the entire optical spectrum, we classify SN 2019neq as a fastevolving SLSN-I having a photospheric velocity gradient of  $\dot{v} \sim 375 \, \mathrm{km \, s^{-1} \, day^{-1}}$ , which is among the highest velocity gradients observed for an SLSN-I. Inferring the velocity gradient from the proposed Fe II  $\lambda 5169$  feature alone would result in  $\dot{v} \sim 100 \, \mathrm{km \, s^{-1}}$  day<sup>-1</sup>, which is still within the observed range of fast-evolving SLSNe-I. In addition, we derive the number density of relevant ionization states for a variety of identified elements at the epoch of the three observations. Finally, we give constraints on the lower limit of the ejecta mass and find that both SLSNe have an ejecta mass at least one order of magnitude higher than normal SNe Ia, while the fast-evolving SN 2019neq has an ejecta mass a factor of two lower than the slowly evolving SN 2010kd. These mass estimates suggest the existence of a possible correlation between the evolution timescale and the ejected mass of SLSNe-I.

*Unified Astronomy Thesaurus concepts:* Supernovae (1668); Core-collapse supernovae (304); Ejecta (453); Atomic spectroscopy (2099); Chemical abundances (224); Astrochemistry (75)

Supporting material: data behind figure

#### 1. Introduction

A revolution in the philosophy and technology of astronomical time-domain surveys has revealed multiple classes of hitherto undiscovered astrophysical transients. For example, using the ROTSE-IIIb telescope at McDonald Observatory in Texas, Quimby et al. (2007) conducted a photometric survey (Quimby 2006) of nearby galaxy clusters in a search for transient sources and discovered a new class of superluminous supernovae (SLSNe).

It has often been reported that SLSNe have absolute peak magnitudes  $M_{\rm AB} < -21$ , total radiated energies of  $\sim 10^{51}$  erg (Gal-Yam 2012), and a strong preference for low-metallicity, star-forming environments (Lunnan et al. 2013, 2014; Leloudas et al. 2015; Angus et al. 2016; Perley et al. 2016; Schulze et al. 2018). Recent studies of homogeneously selected samples of SLSNe (De Cia et al. 2018; Lunnan et al. 2018; Angus et al. 2019) have further highlighted the diversity that is intrinsic in the population. Transients as faint as  $M_r = -19.4$  (e.g., DES14C1rhg; Angus et al. 2019) have been identified as SLSNe due to the similarity of their spectroscopic evolution to known SLSNe (e.g., Quimby et al. 2018). Meanwhile, a handful of SLSNe (PTF10uhf; Perley et al. 2016, SN 2017egm; Chen et al. 2017) have been found to explode in relatively bright late-type galaxies.

Like classical supernova types, SLSNe are divided into two main groups: the hydrogen-rich Type II SLSNe (SLSNe-II) and the hydrogen-poor SLSNe-I classes (Gal-Yam 2012; Branch & Wheeler 2017; Inserra 2019). SLSNe-II are separated into the following subclasses: SLSNe-IIn, with a luminosity evolution powered by an interaction with a massive circumstellar medium (e.g., SN 2006gy; Smith et al. 2007), and normal SLSNe-II, ostensibly without interaction (e.g., SN 2013hx; Inserra et al. 2018). The former have spectroscopic properties similar to traditional Type IIn SNe (Branch & Wheeler 2017).

In this paper, we focus on an SLSN belonging to the more frequently observed hydrogen-poor SLSNe-I. This group is claimed to show some resemblance to Type Ic SNe at late times (Pastorello et al. 2010), even though some SLSNe-I have developed late-time, broad hydrogen emission features (Yan et al. 2015, 2017). SLSNe-I have also been divided into two subgroups (Inserra et al. 2018): the fast-evolving SLSNe-I with an average light-curve rise time of  $\sim$ 28 days (hereafter "Fast SLSNe-I," e.g., SN 2015bn; Nicholl et al. 2016, 2018), and the slowly evolving SLSNe-I with a rise time of  $\sim$ 52 days (hereafter "Slow SLSNe-I," e.g., SN 2011ke; Inserra et al. 2013; Quimby et al. 2018). Inserra et al. (2018) found that Fast SLSNe-I also exhibit high expansion velocities ( $v \ge 1$ 12,000 km s<sup>-1</sup>) and large velocity gradients from 10 to 30 rest-frame days past maximum light, contrary to Slow SLSNe-I, which are characterized by lower expansion velocities ( $v \leq 1$ 12,000 km s<sup>-1</sup>) and negligible velocity gradients from 10 to 30 days post-peak.

The early-phase spectra of SLSNe-I are dominated by the W-like feature around  $\sim$ 4500 Å that is widely accepted as being due to O II (e.g., Liu et al. 2017), although other suggestions also exist (e.g., Quimby et al. 2007). Quimby et al. (2018) presented an in-depth analysis of this region using SYN++ and found evidence supporting the O II hypothesis, which has also been favored by Mazzali et al. (2016) for most of their sample of SLSNe-I. On the other hand, Dessart (2019) presented time-dependent, non-local thermodynamic equilibrium (NLTE) simulations of magnetar-powered SLSN-I spectra and found that in models reaching  $M_V \sim -21$  mag O III and C III features can be as strong as those of O II and C II during the photospheric phase. We explore this ambiguity in Section 4.

In this paper, we present a comparative spectroscopic study of the recently discovered (Nordin et al. 2019) and relatively close SN 2019neq (z=0.1059), which was suggested to belong to the fast-evolving SLSNe-I by Perley et al. (2019) and Thomas et al. (2019), by comparison with the well-observed Slow SLSN-I, SN 2010kd (z=0.101, Vinko et al. 2010; Kumar et al. 2020). Our main goal is to explore the differences between the two groups of SLSNe-I (besides the dissimilarity in the timescale of their light-curve evolution and the differences in their velocity evolution; Inserra et al. 2018). This is a crucial question, because the differences in the spectrum may imply different ejecta.

The slowly evolving SN 2010kd is a good comparison object to SN 2019neq in terms of chemical composition and spectral evolution, since the two SLSNe have similar redshifts, which means similar observational circumstances, e.g., rest-frame spectral coverage, signal-to-noise ratio, effects due to time dilation, etc.

Recently Kumar et al. (2020) performed a detailed study of the photometric and spectroscopic properties of SN 2010kd using the same spectral modeling technique that we apply in the present paper, which gives further motivation for the comparison with SN 2019neq.

In Section 2, we describe our new spectroscopic observations of SN 2019neq, then in Section 3 we present its classification based on its spectral and velocity evolution. In Section 4 we present detailed spectroscopic modeling of SN 2019neq with the code SYN++ (Thomas et al. 2011).

In Section 5.1 we infer the number densities of the identified elements for each detected ionization state, and in Section 5.2 we compare the spectroscopic evolution of SN 2010kd and SN 2019neq. We estimate the total mass ejected during the explosion in Section 5.3. We conclude in Section 6.

#### 2. Observations

SN 2019neq was discovered (R.A. = 17:54:26.736, decl. = +47:15:40.56) by the Zwicky Transient Facility (ZTF; Bellm et al. 2019) public survey on 2019 August 10 at 05:25:45 UT in the ZTF g-band at  $g=19.78\pm0.24$  AB-magnitude and given the internal designation ZTF19abpbopt. An r-band observation of the same field on 2019 August 10 at 04:44:43 UT did not detect significant flux above the limit of r=20.30 AB-magnitude. The last non-detection in the g-band occurred on 2019 August 8 at 07:29:09 UT (MJD 58703.312). SN 2019neq was first reported to the Transient Name Server (TNS) on 2019 August 11 (Nordin et al. 2019). Significant flux in the ZTF r-band was first detected on 2019 August 13.

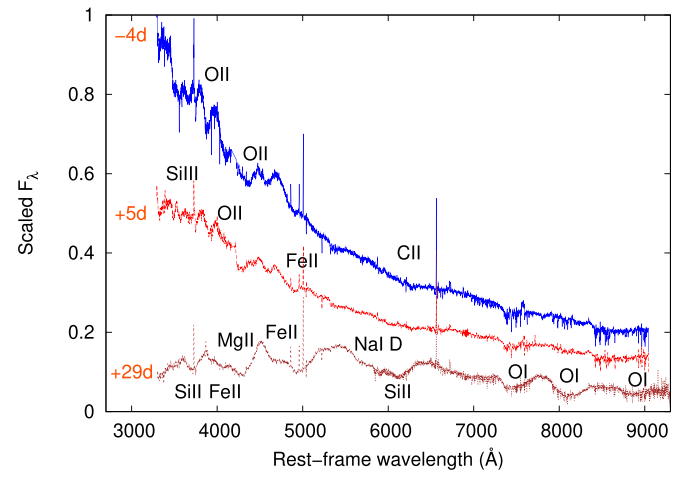


**Figure 1.** The observed spectra of SN 2019neq at phases -4, +5, and +29 days from maximum. Feature identifications are based on spectroscopic modeling with SYN++ presented in Section 4.

(The data used to create this figure are available.)

A series of spectral observations were obtained by the SED Machine between 2019 August 11 and 22, exhibiting a featureless blue continuum. A  $2 \times 900 \,\mathrm{s}$  spectrum was obtained by SPRAT on the Liverpool Telescope on 2019 August 27 (Perley et al. 2019), showing narrow emission lines from the host galaxy at a redshift of z = 0.1075, superimposed on a blue continuum with broad, weak absorption features. This early spectrum was analyzed with superfit, which gave a good match to an SLSN-I before maximum light.

Here we present three optical spectra (3640  $\leqslant \lambda \leqslant$  10000 Å) of SN 2019neq (first reported by Thomas et al. 2019), taken with the Low Resolution Spectrograph-2 (LRS2; Chonis et al. 2016) mounted on the 10 m Hobby–Eberly Telescope (HET) at McDonald Observatory in Texas. We obtained these spectra on 2019 September 1, 11 and 2019 October 6/8. Each of these observations was carried out in both the blue (LRS2-B: 3640–6970 Å) and red (LRS2-R: 6440–11000 Å) arms of LRS2, with 1800 s integration times per arm for the first two observations. The third observation was split between two nights due to non-ideal weather conditions, and exposed for 2100 s because the target had faded significantly.

Spectroscopic reductions were executed using the automated spectroscopic reduction tool Panacea. The fully reduced HET/LRS2 spectra are presented in Figure 1. These spectra were corrected for redshift and interstellar extinction. The data will be available on the Weizmann Interactive Supernova Data Repository (WISeREP<sup>8</sup>).

To determine the date of maximum light, we use Gaussian processes to interpolate the public ZTF light curve of SN 2019neq downloaded from the Lasair<sup>9</sup> website (Smith et al. 2019), and the flux uncertainty therein, as shown in Figure 2. We use the ZTF *g*-band maximum to define the peak of the light curve. The spectral energy distribution of this nearby SLSN-I, had it been observed, would contain more flux

https://wis-tns.weizmann.ac.il/object/2019neq

<sup>6</sup> https://github.com/dahowell/superfit

https://github.com/grzeimann/Panacea/

https://wiserep.weizmann.ac.il/

https://lasair.roe.ac.uk/object/ZTF19abpbopt/

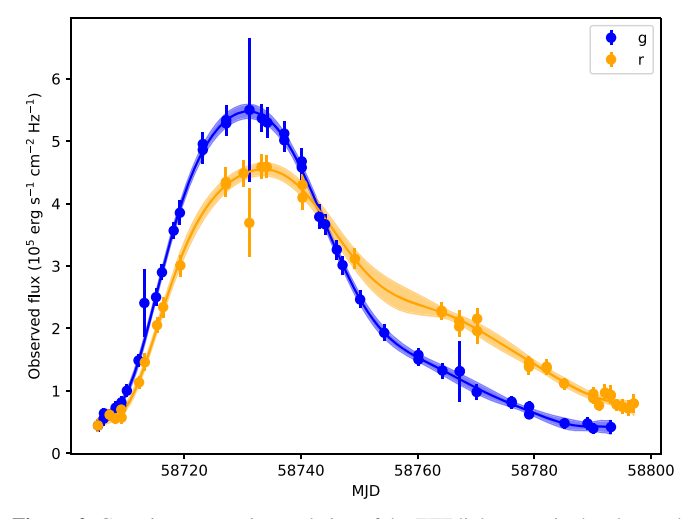


**Figure 2.** Gaussian process interpolation of the ZTF light curve in the observed frame. The interpolated light curve is used to find the epoch of maximum light in the *g*-band, and thereby the relative phase of our HET spectra.

in the g-band than in the r-band (the ZTF public survey is restricted to these two bandpasses).

We use an exponential sine-squared kernel to perform the Gaussian process fit. Some authors (e.g., Inserra et al. 2018; Angus et al. 2019) have found that the more complex Matern 3/2 kernel is well suited to approximate fluctuations at short timescales in the observed SLSN flux. In this work, however, we use Gaussian processes exclusively to determine the epoch of maximum light, and find that the exponential sine-squared kernel is sufficient. We determine the epoch of maximum light of our interpolated light curve to be 58731 (MJD), and adopt this value hereafter.

To estimate the explosion date we fit an  $L \sim t^2$  light-curve model to the first two weeks of the ZTF g-band light curve. We obtain  $t_{\rm exp} \sim 58700.7$  MJD as the likely explosion date, and we assign  $\pm 2$  days as a conservative estimate for its uncertainty.

The basic observational data of SN 2019neq are presented in Table 1, alongside those of our comparison object SN 2010kd. A detailed comparison of the spectroscopic evolution of these two objects is given in Section 5.2.

#### 3. Classification

In the left panel of Figure 3, the first spectrum of SN 2019neq, taken at a phase of −4 days, or four rest-frame days before maximum light, is compared to a spectrum of the Type I SLSN SN 2005ap, which was taken at a similar phase of −2 days (Quimby et al. 2007). The similarity of the two spectra is apparent, as was noted by Perley et al. (2019). Both spectra were obtained slightly before maximum, and they both show the W-shaped feature at ~4300 Å. This feature is often used to identify SLSNe I at early times, because it is not present in normal Type Ic or Ic-BL (broad-lined) events (Liu et al. 2017). The spectral similarity shown in Figure 3 strongly suggests that SN 2019neq is an SLSN-I around maximum light. The chemical composition of SN 2019neq, especially the lack of H and He features, provides further evidence that SN 2019neq is a Type I SLSN that is similar to SN 2005ap.

The right panel of Figure 3 compares the public *r*-band ZTF light curve (filled red dots) of SN 2019neq to the *R*-band light curve of the Fast SLSN-I SN 2005ap (Quimby et al. 2007; blue

triangles), and the Slow SLSN-I SN 2010kd (Kumar et al. 2020; empty green circles). As expected from the spectral similarity between SN 2019neq and SN 2005ap, they have similar light curves, while the timescale of the light-curve evolution of SN 2010kd is nearly a factor of 2 slower. This fact establishes that SN 2019neq belongs to the Fast SLSN-I group as defined by light-curve behavior.

In order to classify SN 2019neq based on its photospheric velocity evolution, we follow the procedure of Inserra et al. (2018); we fit a Gaussian profile to the absorption minimum identified as that belonging to the Fe II  $\lambda 5169$  line, where the mean of the Gaussian distribution represents the center of the absorption profile. We measure the blueshift from the emitted-frame wavelength of 5169 Å, which indicates the photospheric velocity along our line of sight. We remove narrow galaxy emission lines from the fit.

As can be seen in the upper panel of Figure 4, the blueshifted Fe II absorption profile of SN 2019neq is well modeled by a Gaussian distribution. The posterior distribution of the fit to the -4 days spectrum is shown in the lower panel of Figure 4. Here,  $\mu$  and  $\sigma$  represent the position and width of the Gaussian function. There are two additional nuisance parameters that set the amplitude and baseline.

To derive the uncertainty on the Fe II velocity, we select the 16th, 50th, and 84th percentiles of the posterior distribution in  $\mu$ . It is not appropriate to derive the uncertainty from the posterior on  $\sigma$ , because (1) this represents the (equivalent) width of the absorption profile, which is related to physical quantities other than the line-of-sight velocity of matter at the photosphere, and (2) a significant contribution to the local flux deficit may be present due to nearby absorption features not originating from Fe II  $\lambda 5169$  (see Section 4).

We find photospheric velocities of  $15,900 \pm 140 \, \mathrm{km \, s^{-1}}$ ,  $16,500 \pm 150 \, \mathrm{km \, s^{-1}}$ , and  $14,100^{+80}_{-120} \, \mathrm{km \, s^{-1}}$  at spectroscopic phases of -4, +5, and +29 rest-frame days from maximum light. These measurements imply a velocity gradient of  $\dot{v} = \Delta v/\Delta t = 2400^{+170}_{-190}/24 = 100^{+7}_{-8} \, \mathrm{km \, s^{-1} \, day^{-1}}$  from 5 to 29 rest-frame days after peak, which is within the range of the observed velocity gradients of Fast SLSNe-I (Inserra et al. 2018). This establishes that SN 2019neq belongs to the group of Fast SLSNe-I *as defined by spectroscopic characteristics*.

A caveat to the Gaussian-fitting technique for photospheric velocity measurements has been presented by Modjaz et al. (2016), who pointed out that "line velocities" determined in this way may not represent the true photospheric velocity for SLSNe (or indeed any SN with sufficiently broad line profiles, such as SNe Ic-BL). The features of such SNe are usually complex blends of several lines. This is true for the Fe II  $\lambda 5169$  feature in particular, which is blended with Fe II  $\lambda 4924$  and  $\lambda 5018$  (Modjaz et al. 2016). Thus, we emphasize that we use the Fe II  $\lambda 5169$  line "velocities" only as a diagnostic tool to distinguish between the spectroscopically "Fast" and "Slow" SLSNe-I, following the methodology of Inserra et al. (2018), and do not consider these velocities as representatives of the true photospheric velocity. A more thorough velocity measurement will be presented in Section 4.

In Figure 5, we compare the +29 days spectrum of SN 2019neq to that of the Slow SLSN-I SN 2010kd taken at +85 days phase (Kumar et al. 2020). Fast SLSNe-I are expected to reach the same spectroscopic phase earlier than Slow SLSNe-I. We visually inspected the observed spectra of SN 2010kd presented by Kumar et al. (2020) to find the one

Table 1
Basic Data of the Studied SLSNe

SN	R.A.	Decl.	Discovery	Explosion (MJD)	t <sub>max</sub> (MJD)	m <sub>max</sub> [BAND] (mag)	z	$E(B-V)_{MW}$
SN 2010kd	12:08:01 (a),	+49:13:31 (a),	2010 Nov 14	55499.5 (d)	55552.0 (e)	16.16 [U] (e)	0.1010	0.0197 (f)
SN 2019neq	(b), (c) 17:54:26 (g)	(b), (c) +47:25:40 (g)	(a), (b) 2019 Aug 10 (g)	58700.7 (h)	58731.0 (h)	17.79 [i] (h)	(a), (b) 0.1059 (i)	0.0330 (f)

**References.** (a) Lennarz et al. (2012); (b) Vinko et al. (2010); (c) Barbon et al. (2008); (d) Kumar et al. (2020); (e) Brown et al. (2014); (f) Schlafly & Finkbeiner (2011); (g) Nordin et al. (2019); (h) present paper; (i) calculated from narrow H $\alpha$  emission from the host.

that best resembled the +29 days spectrum of SN 2019neq. Among the SN 2010kd spectra taken at +34, +85, +96, +144, and +194 days rest-frame phases, the +85 days spectrum was found to be most similar to the +29 days spectrum of SN 2019neq.

From Figure 5 it is apparent that the main absorption troughs and pseudo-emission peaks of the two spectra are quite similar, in spite of their different phases and Doppler shifts. This shows that SN 2019neq reached a physical state at  $\sim+30$  days similar to that of SN 2010kd at +85 days. This confirms the fast spectral evolution of SN 2019neq and strengthens its classification as a Fast SLSN-I. Note that in the SN 2010kd spectrum some nebular emission features (e.g., [O I]  $\lambda\lambda6300$ , 6363; [Ca II]  $\lambda\lambda7291$ , 7323) appear (Kumar et al. 2020), which suggest the dilution of the ejecta and strengthening of the NLTE conditions in the envelope (the feature identifications for SN 2019neq are from Section 4).

#### 4. Spectrum Modeling

To model the available photospheric-phase spectra of SN 2019neq, we used the SYN++ (Thomas et al. 2011) code, which is the revised and improved version of the FORTRAN code SYNOW (Fisher 2000; Hatano et al. 1999).

SYN++ requires global parameters referring to the whole model spectrum, and local parameters to fit the lines of the individual elements. The global parameters are the following:

- 1.  $a_0$ : a constant multiplier to the whole model spectrum
- 2.  $v_{\text{phot}}$ : velocity at the photosphere
- 3.  $\hat{T}_{phot}$ : temperature at the photosphere.

## The local parameters are

- 1.  $\tau$ : optical depth for the reference line of each ion
- 2.  $v_{\min}$ : the inner velocity of the line-forming region
- 3.  $v_{\text{max}}$ : the outer velocity of the line-forming region
- 4.  $\sigma$ : scale height of the optical depth above the photosphere in km s<sup>-1</sup>. This parameter is responsible for the width of the spectral features, which is roughly related to the width of the line-forming region in the atmosphere. A larger  $\sigma$  parameter implies a broader feature.
- 5.  $T_{\rm exc}$ : excitation temperature of each element, assuming local thermodynamic equilibrium (LTE). Different ions may have different  $T_{\rm exc}$  parameters, mimicking NLTE conditions.

It can be seen in Figure 1 that during the photospheric phase the spectra of SN 2019neq were dominated by a hot, blue continuum with strong, overlapping P Cygni features (although the presence of emission lines due to NLTE effects cannot be ruled out). Since there is no single, unblended feature in these spectra, a spectral synthesis code is necessary to determine the

chemical composition of the ejecta reliably, even under LTE conditions (Branch & Wheeler 2017) which are assumed here.

To examine the evolution of the temperature and photospheric velocity of SN 2019neq, and firmly identify P Cygni lines, we modeled all three of our LRS2 spectra.

The global parameters for the best-fit models are collected in Table 2, while the list of the local parameters for each ion can be found in Table A1 in the Appendix.

The observed spectrum and its best-fit model for the first epoch (at phase -4 days) can be seen in Figure 6. The observed spectrum contains strong, narrow  $H\alpha$   $\lambda6562.8$  and forbidden [O III]  $\lambda\lambda4932$ , 4960, 5008 lines due to the host galaxy. The redshift of SN 2019neq was calculated by fitting a Gaussian profile to the narrow  $H\alpha$  feature, resulting in  $z=0.105942\pm0.000006$ , as presented in Table 1.

At this early phase, the photospheric temperature implied by the SYN++ model is  $\sim$ 15,000 K, while the model expansion velocity is also very high (21,000 km s<sup>-1</sup>) compared to normal Type Ia or core-collapse SNe. A normal Type Ia SN has photospheric velocity of  $\sim 10,000 \,\mathrm{km \, s^{-1}}$  around maximum (e.g., Jha et al. 2019), while the typical value for core-collapse SNe at about  $\sim 1$  month after maximum is  $\sim 5000 \, \mathrm{km \, s^{-1}}$  (e.g., de Jaeger et al. 2019). The photospheric velocity of SN 2019neq is similar to the high-velocity component of the strong Ca II features that are frequently identified in the premaximum spectra of SNe Ia (e.g., Silverman et al. 2015; Mulligan et al. 2019). According to Inserra et al. (2018),  $21,000 \,\mathrm{km}\,\mathrm{s}^{-1}$  is about a factor of 2 higher than the typical photospheric velocity of Slow SLSNe-I (~9000 km s<sup>-1</sup>), but it is close to the observed upper limit for Fast SLSNe-I ( $v_{\rm phot} \lesssim$  $20,000 \,\mathrm{km \, s^{-1}}$  at  $\sim 10$  days after maximum; see Figure 7 in Inserra et al. 2018).

As noted in the introduction, the W-like feature appearing between 4300 and 4500 Å is often adopted as an identifying spectral characteristic of SLSN-I. This feature seems to be somewhat weaker in SN 2019neq than in SN 2005ap and other SLSNe-I shown in Quimby et al. (2018). To illustrate this difference quantitatively, we derived the equivalent width (EW) of this feature using the splot task in IRAF $^{10}$  (Image Reduction and Analysis Facility). We obtained EW = 32.01 Å and 89.85 Å for SN 2019neq and SN 2005ap respectively. The W-shaped feature is thus weaker by a factor of  $\sim\!\!3$  in SN 2019neq than in SN 2005ap.

Our first model, plotted in Figure 6, contains C II, C III, O III, Si III, Si IV, Co III, and Fe II lines (optical depths and other parameters are summarized in Tables A1–A3 in the Appendix). In this model the W-shaped feature can be

<sup>&</sup>lt;sup>10</sup> IRAF is distributed by the National Optical Astronomy Observatories, which are operated by the Association of Universities for Research in Astronomy, Inc., under cooperative agreement with the National Science Foundation <a href="https://iraf.noao.edu">http://iraf.noao.edu</a>.

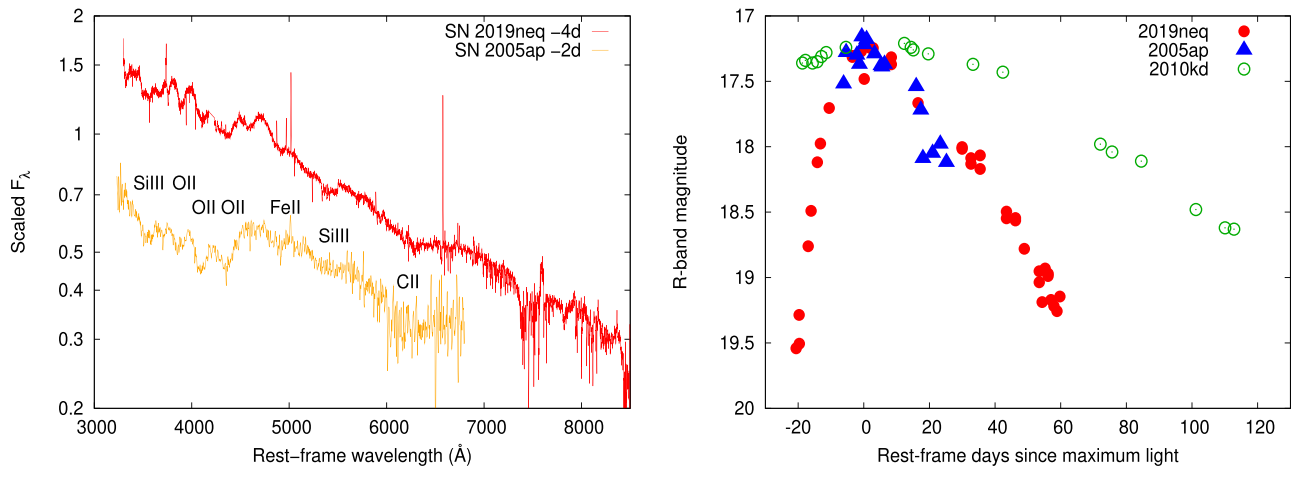


Figure 3. Left panel: comparison of the pre-maximum spectra of SN 2019neq -4 days (red) and SN 2005ap -2 days (orange). The general similarity of the two spectra is apparent. The identifications of the apparent features are based on syn++ modeling of SN 2019neq (Section 4). Right panel: comparison of the light curves of SN 2019neq (red), SN 2005ap (blue), and SN 2010kd (green). The light curves are shifted together to a common maximum light. SN 2019neq and SN 2005ap both show faster light curves, while SN 2010kd evolves more slowly than them.

explained by the combination of C III, O III, Si III, and Co III multiplets, similar to the results of Quimby et al. (2007). Alternatively, the spectrum can also be fit using O II instead of O III, C III, and Si IV as shown in the left panel in Figure 7. The comparison of these two models is plotted in the right panel of Figure 7, where our first SN 2019neq spectrum (red line) is plotted, together with the two SYN++ models. The labels A, B, C, D, and E mark the same features as in Quimby et al. (2018) (see their Figure 13). The two simple SYN++ models reproduce these features equally well, although neither model accounts for the pseudo-emission around ~4700 Å that is present in SN 2019neq.

Even though the "O II model" provides a more elegant explanation for four out of five observed features with a single ion, the validity of the "O III model" cannot be ruled out in the relatively hot ejecta of SN 2019neq. According to Hatano et al. (1999), the optical depths for O II and C II expected in an atmosphere having  $T \sim 15,000$  K are the same as for O III and C III. It is therefore possible that doubly ionized ions also play a role in the formation of the spectrum of SN 2019neq between 3500 and 4500 Å. This is also in agreement with Dessart (2019), who showed that in the brightest, hottest magnetar-driven SLSNe-I ejecta, where the NLTE effects are minimal around maximum light, both O II/C II and O III/C III features may appear in the optical spectra.

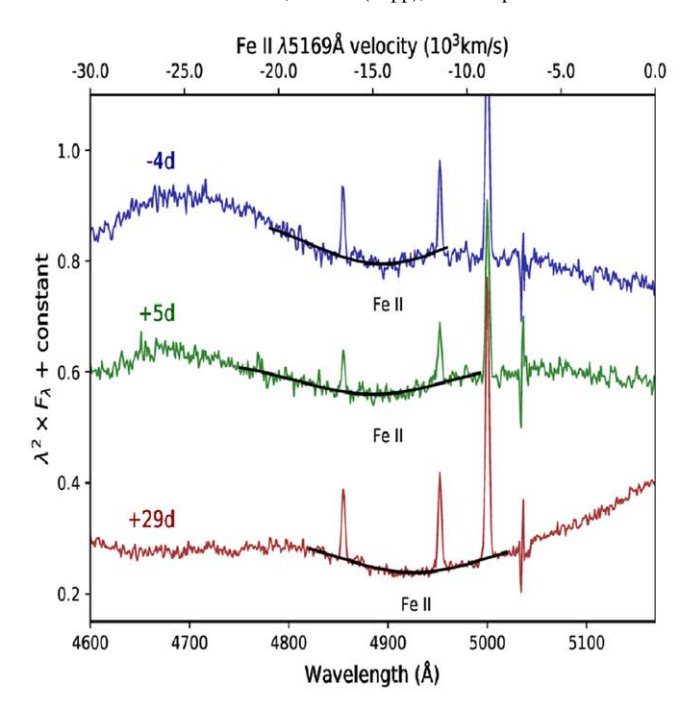
Although both models can describe the observed features well, the true chemical composition of the ejecta remains uncertain because of the relatively high photospheric temperature. Since these models are built using the same elements (C, O, and Si), but with different excitation, the selection of the O II or O III model would not cause a dramatic distinction in the chemical composition of the ejecta.

The second spectrum of SN 2019neq was taken at +5 days after maximum light. Figure 8 shows the best-fit SYN++ model to this spectrum. This new model implies that the photospheric temperature had decreased to 12,000 K, and lines of C I had appeared (unlike in the previous spectrum). In the left panel of Figure 8, two alternative models can be seen, having the same local and global parameters but different photospheric velocities.

The ambiguity of  $v_{\rm phot}$  is caused by the identification of the features around 5000 Å thought to be due to Fe II. If we assigned the minimum of the observed feature (shown by the dashed vertical line in the inset of the left panel of Figure 8) to the Fe II  $\lambda 5169$  transition (see Section 3) then the photospheric velocity would be  $16,000\,\mathrm{km\,s^{-1}}$ . Accordingly, our first model for this spectrum was built with  $v_{\mathrm{phot}} = 16,000\,\mathrm{km\,s^{-1}}$  (plotted in blue in the left panel of Figure 8). A second model was then developed using the criterion that the absorption minima of all identified features are fit optimally, implying  $v_{\mathrm{phot}} \sim 21,000\,\mathrm{km\,s^{-1}}$ , which is shown by the red line in the left panel of Figure 8. The model with a higher photospheric velocity matches the data more accurately than the slower model. The right panel of Figure 8 presents the ion contributions to the best-fit model.

To further explore this ambiguity, we modeled the Fe II lines with a range of values of the  $\sigma$  parameter in the vicinity of 5000 Å, as shown in Figure 9. The orange line denotes  $\sigma = 2000 \, \mathrm{km \, s^{-1}}$ , utilized in the model having  $v_{\mathrm{phot}} = 16,000 \, \mathrm{km \, s^{-1}}$ . The blue lines gives another model having  $\sigma = 300 \, \mathrm{km \, s^{-1}}$ . The dashed vertical line shows the supposed wavelength of the Fe II  $\lambda 5169$  absorption minimum corresponding to  $v_{\rm phot} = 16{,}000 \, {\rm km \, s^{-1}}$ . The feature assumed to be a strong Fe II  $\lambda 5169$  absorption line is actually a blend of many weak features, as pointed out by Modjaz et al. (2016). The small humps on the blue curve correspond to these individual Fe II transitions, which become blended with each other on the orange curve when the widths of the features are broader (indicated by the higher  $\sigma$  parameter). It is clear that the Doppler-shifted position of the Fe II  $\lambda 5169$  (dashed vertical line) differs from the wavelengths of the minima of the two model spectra. We conclude that the broad feature observed around 5000 Å cannot be interpreted simply as due to Fe II  $\lambda$ 5169. This is the primary reason why the model with lower  $v_{\rm phot}$  value does not fit the absorption minima of the other lines in the +5 days phase spectrum of SN 2019neq. A better estimate for  $v_{\text{phot}}$  can be obtained by fitting the whole spectrum with a model that (ideally) takes into account all observed spectral features.

Since the model having  $v_{\text{phot}} = 21,000 \,\text{km s}^{-1}$ , which is based on fitting the observed spectrum as a whole, describes the



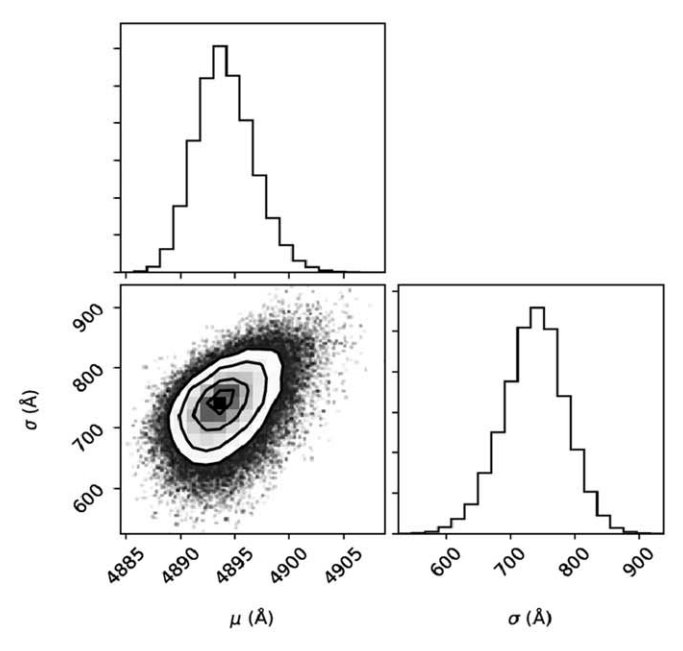


**Figure 4.** Top: best fitting Gaussian distributions to the Fe II  $\lambda 5169$  absorption profiles in our three spectra of SN 2019neq. The implied photospheric velocity is shown on the top horizontal axis. The narrow emission lines that can be seen in all spectra are from the host galaxy. Bottom: 2D posterior distribution of parameters from the Gaussian fit to our SN 2019neq spectrum at -4 rest-frame days. Here,  $\mu$  is the center of the Fe II  $\lambda 5169$  absorption profile, while  $\sigma$  is its width.

data better than the model with  $v_{\rm phot}=16,000\,{\rm km\,s^{-1}}$ , which is obtained from the Doppler shift of the single (assumed) Fe II  $\lambda 5169$  feature, we adopted  $v_{\rm phot}=21,000\,{\rm km\,s^{-1}}$  as the photospheric velocity of the best-fit model to the +5 days spectrum.

Note that Modjaz et al. (2016) reached a very similar conclusion regarding line blending and suggested fitting an artificially broadened sequence of phase-dependent template SN Ic spectra to the observed SLSN-I spectrum to find a

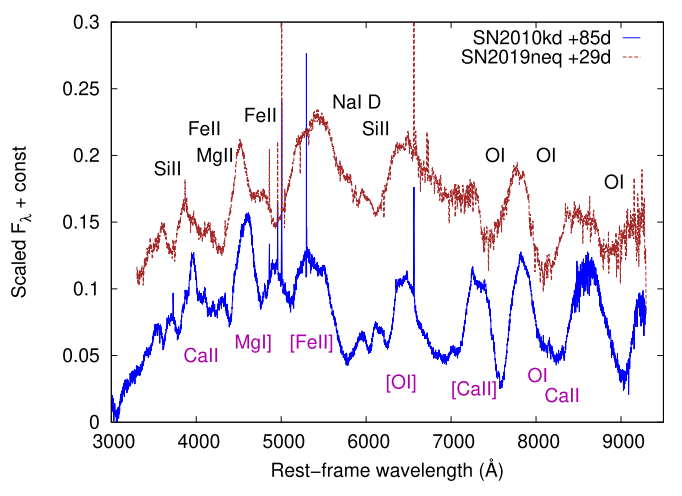


**Figure 5.** Spectral comparison of SN 2010kd at +85 days phase (blue line) and SN 2019neq at +29 days (brown line). Feature IDs are based on syn++ modeling of SN 2019neq (black, see Section 4) and synapps modeling of SN 2010kd (purple, see Kumar et al. 2020). The overall similarity of the two spectra is apparent in spite of their different phases. This confirms the fast spectral evolution of SN 2019neq.

 Table 2

 Best-fit Global Parameters of the SYN++ Photospheric-phase Models of SN 2019neq

MJD (days)	Phase (days)	$a_0$	$(\text{km s}^{-1})$	$T_{\rm phot}$ $(10^3 \text{ K})$
58727	-4	0.24	21 000	15.0
58737	5	0.13	21 000	12.0
58763	29	0.14	12 000	6.0

relative estimate of the true  $v_{\rm phot}$ . We found that their approach does not work well for SN 2019neq. Even though the spectra of SLSNe-I are somewhat similar to those of SNe Ic, there are too many differences between the observed and the template spectra around 5000 Å that prevent the unambiguous fitting of the latter to the former. Building a full, parameterized SYN++ model, although more time-consuming, was found to produce better fits and more realistic  $v_{\rm phot}$  estimates.

Based on the spectrum taken at  $\sim 1$  month after maximum, Thomas et al. (2019) reported that SN 2019neq exhibited very fast spectral evolution. This can be seen in Figure 10, where the third spectrum, taken at +29 days phase is plotted together with its best-fit SYN++ model. From +5 to +29 days the photospheric velocity obtained from the SYN++ spectrum modeling decreased from 21,000 to 12,000 km s $^{-1}$ , and the temperature at the photosphere diminished from 12,000 to 6000 K. In accordance with the decreasing temperature, the low-ionization elements began to dominate the highly excited ones. We identified the presence of O I, Na I, Mg II, Si II, and Fe II lines, as can be seen in Figure 10 (see also Table 2).

From the  $v_{\rm phot}$  values derived from our SYN++ models of the +5 days and the +29 days spectra, a better estimate of the true velocity gradient can be inferred. We find  $\dot{v} = \Delta v/\Delta t \sim 9000/24 \sim 375\,{\rm km\,s^{-1}}\,{\rm day^{-1}}$ , which is a factor of ~4 higher than the value  $\dot{v} \sim 100\,{\rm km\,s^{-1}}\,{\rm day^{-1}}$  found in Section 3. This velocity gradient would put SN 2019neq in the range of the Fast SLSNe-I in the sample of Inserra et al. (2018), with one of the highest  $\dot{v}$  parameters. We note, however, that the methodology for measuring  $\dot{v}$  used by Inserra et al. (2018) is different from ours: they applied the single-Gaussian fitting

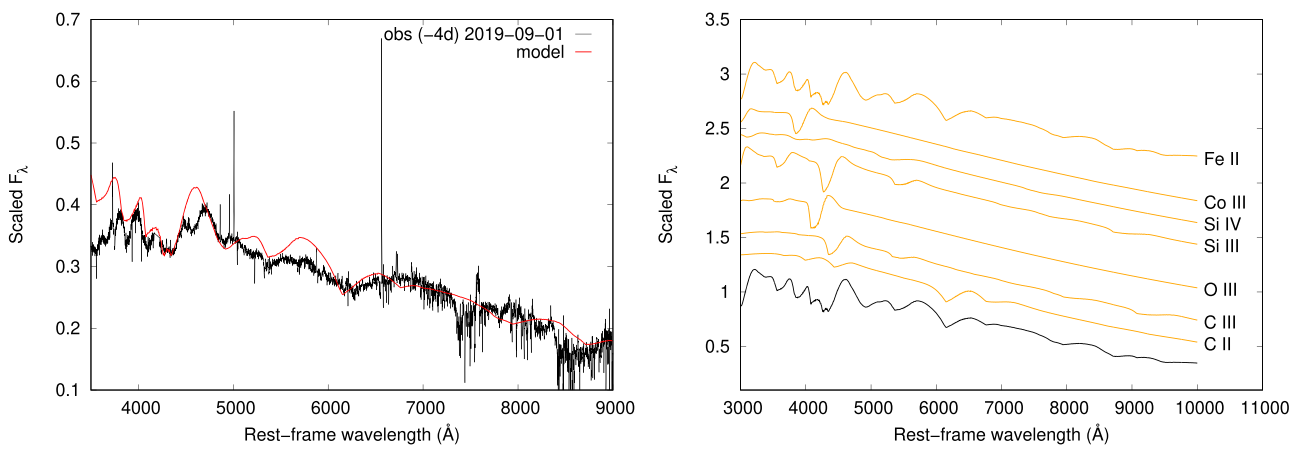
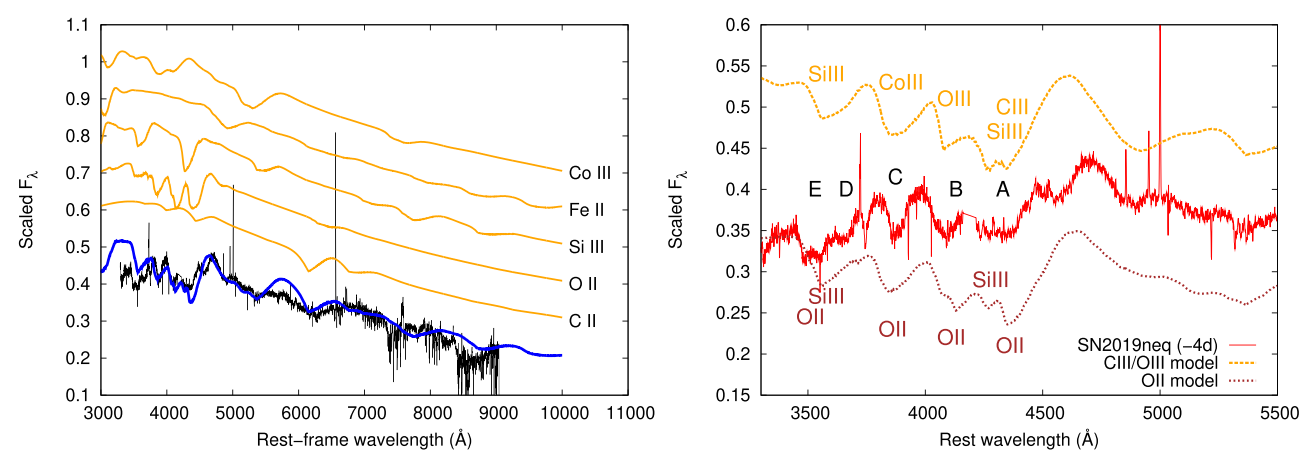


Figure 6. Left panel: the observed (black line) spectrum of SN 2019neq at phase -4 days (2019 September 1) plotted together with the best-fit model obtained with SYN++ (red line).  $\lambda^2 F_{\lambda}$  is plotted on the vertical axis. Right panel: single-ion contributions (orange lines) to the overall model spectrum (black line).



**Figure 7.** Left panel: the alternative model of the -4 days spectrum of SN 2019neq, where the W-shaped feature between 4300 and 4500 Å is fitted with O II instead of O III, C III, and Si IV. Right panel: comparison of the two models (orange and brown curves) with the -4 days spectrum of SN 2019neq (red). The models have been shifted vertically for clarity, and all spectra have had their continua flattened. Ion identifications are from SYN++.

method, which gives  $\dot{v} \sim 100 \, \mathrm{km \, s^{-1}} \, \mathrm{day^{-1}}$  for SN 2019neq (see Section 3). Our classification of SN 2019neq as a Fast SLSN-I is robust with respect to the method used to measure the velocity evolution.

#### 5. Discussion

# 5.1. Inferring the Number Density of the Ionization States in the Ejecta of SN 2019neq

From the SYN++ model parameters listed in Tables 2 and A1, we estimated the number and mass densities of the identified ions in each spectrum, following Hatano et al. (1999).

According to the Sobolev approximation (e.g., Hatano et al. 1999), the optical depth of a P Cygni feature can be expressed as

$$\tau = \left(\frac{\pi e^2}{m_e c}\right) f \lambda t n_l \left(1 - \frac{g_l n_u}{g_u n_l}\right),\tag{1}$$

where  $n_u$  and  $n_l$  refer to the number densities of the particular ion at the upper and lower levels of the transition,  $g_u$  and  $g_l$  are the statistical weights, f is the oscillator strength, t is the restframe time since explosion, e and  $m_e$  are the charge and the mass of an electron, and c is the speed of light.

The LTE conditions adopted by SYN++ imply that

$$\frac{n_u}{n_l} = \frac{g_u}{g_l} e^{-\frac{(E_u - E_l)}{kT}}.$$
 (2)

Here,  $E_u$  and  $E_l$  are the energies of the upper and lower levels, and T is the excitation temperature.

From Equations (1) and (2), we can calculate the optical depth as

$$\tau = 0.026 f \lambda_{\mu} t_d n_l (1 - e^{-\frac{hc}{\lambda kT}}), \tag{3}$$

where  $\lambda_{\mu}$  is the wavelength of a particular feature in  $\mu$ m, and  $t_d$  is the number of rest-frame days from explosion.

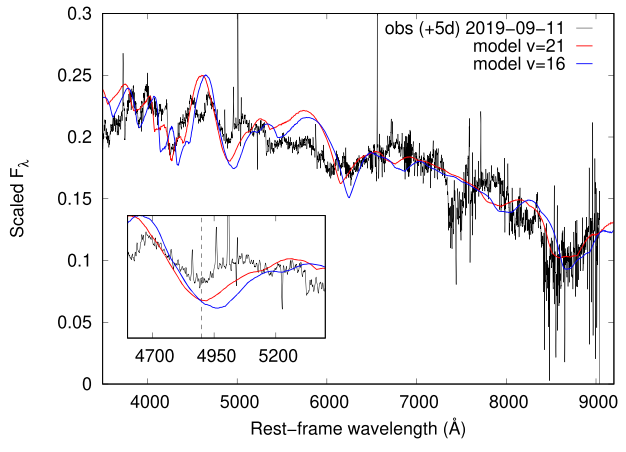
The value of  $n_l$  can then be expressed as

$$n_l = \frac{\tau}{0.026 f \lambda_{ll} t_d (1 - e^{-\frac{hc}{\lambda kT}})} \,. \tag{4}$$

To get the full number density of an element, we can apply the alternative form of the Boltzmann formula (Equation (2)):

$$\frac{n_l}{N} = \frac{g_l}{z(T)} e^{-\frac{\chi}{kT}},\tag{5}$$

where N denotes the full number density of an ion in cm<sup>-3</sup>, z(T) is the partition function,  $\chi = E_l - E_0$  is the excitation potential



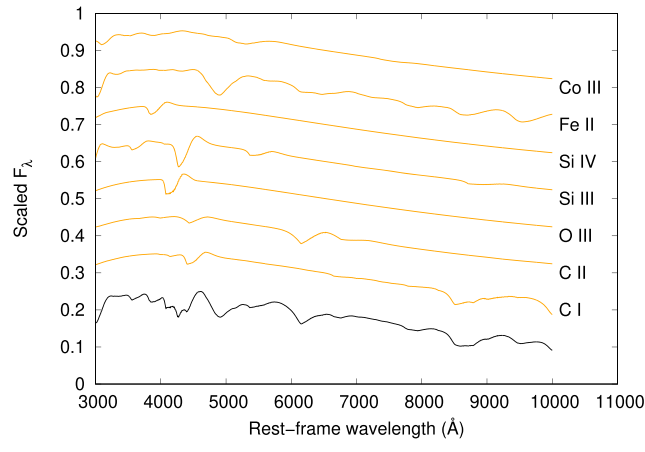
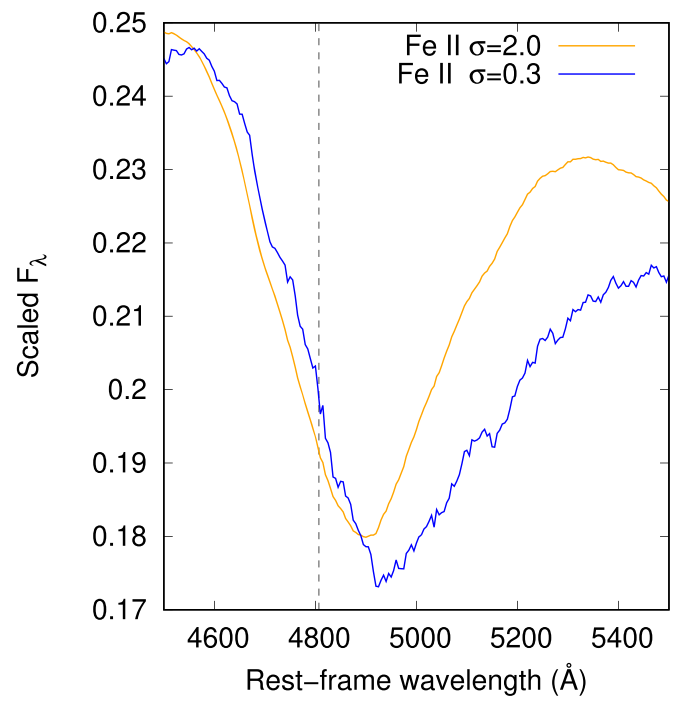


Figure 8. The observed and modeled spectra of SN 2019neq at +5 days phase (2019 September 11). Left panel: the blue line shows a model with  $v_{phot} = 16,000 \text{ km s}^{-1}$ , and the red line denotes the best-fit model with  $v_{phot} = 21,000 \text{ km s}^{-1}$ . The inset zooms in on the Fe II  $\lambda 5169$  feature. The absorption minimum of the red model is much closer to the observed minimum of this line, as indicated by the dashed vertical line in the inset. Right panel: single-ion contributions to the overall model spectrum. The color coding is the same as in Figure 6.



**Figure 9.** SYN++ models of the Fe II  $\lambda 5169$  feature, assuming  $v_{\rm phot}=16,000~{\rm km~s^{-1}}$ . Different colors refer to different values of the  $\sigma$  parameter, and the dashed line shows the wavelength of the ostensible absorption minimum of Fe II  $\lambda 5169$ , Doppler-shifted to  $v_{\rm phot}=16,000~{\rm km~s^{-1}}$ . The wavelengths of the minima of the two model spectra are different from the position of the vertical line, suggesting that this broad feature is not due to a single line of Fe II  $\lambda 5169$ .

of the lower level (in eV), and T is the excitation temperature (in K).

From Equation (5) the total number density (N) can be inferred as

$$N = \frac{n_l z(T)}{g_l} e^{\frac{5040}{T}\chi}, \qquad (6)$$

where  $n_l$  is given by Equation (4) and the temperature in the exponential is measured in K.

From the equations above, the density of each ionization state (in g cm<sup>-3</sup>) can be calculated as the product of the full number density and the ion mass.

In the case of SN 2019neq, the inferred  $n_l$  and N values, as well as the densities for each identified ionization state, can be found in Table A3 in the Appendix. The required data for these calculations are shown in Table A2 in the Appendix. The quantities  $\tau$  and T come from the SYN++ model file, while the atomic data are collected from Hatano et al. (1999) and the National Institute of Standards and Technology (NIST) Atomic Spectra Database. <sup>11</sup>

Note that the ion densities for O II and O III were omitted from Tables A2 and A3, because the reference lines for these ions are forbidden transitions (see Table 2 in Hatano et al. 1999). Since SYN++ calculates the occupation numbers of the different atomic levels assuming LTE, we found that this leads to very high uncertainties in the inferred number densities when the reference lines are forbidden, probably due to the breakdown of the LTE assumption for such transitions.

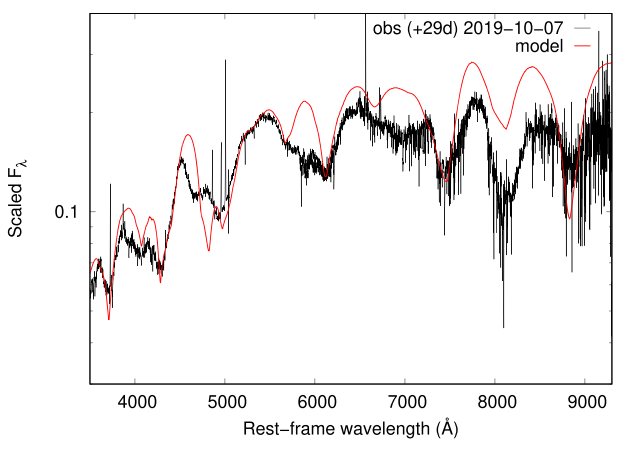
We conclude that the identified ions and their number densities belonging to the first and second epochs (-4 and +5 days), respectively) are quite similar. In contrast, the third spectrum (taken at +29 days) contains a variety of different species, and thus the calculated densities are also different. This may suggest that the inner region of the ejecta, revealed by the spectra at later epochs, is richer in heavier elements than the outer region. A deeper physical interpretation would need more detailed NLTE modeling of photospheric as well as nebular phase spectra, which is beyond the scope of this paper.

#### 5.2. Comparing the Spectral Evolution with the Slow SLSN-I SN 2010kd

In this subsection we compare the spectral evolution of the Fast SLSN-I, SN 2019neq, with the representative Slow SLSN-I, SN 2010kd. The spectroscopic modeling of SN 2010kd, computed with SYNAPPS (SYN++ coupled with an automated parameter optimization routine), was published recently by Kumar et al. (2020).

Figure 11 presents comparisons of the evolution of various spectroscopic quantities. Spectra of the two SLSNe taken before or shortly after maximum light are shown in the top left panel with major features identified by the SYN++ models. It can be seen that the pre-maximum spectra are globally similar:

<sup>11</sup> https://www.nist.gov/pml/atomic-spectra-database



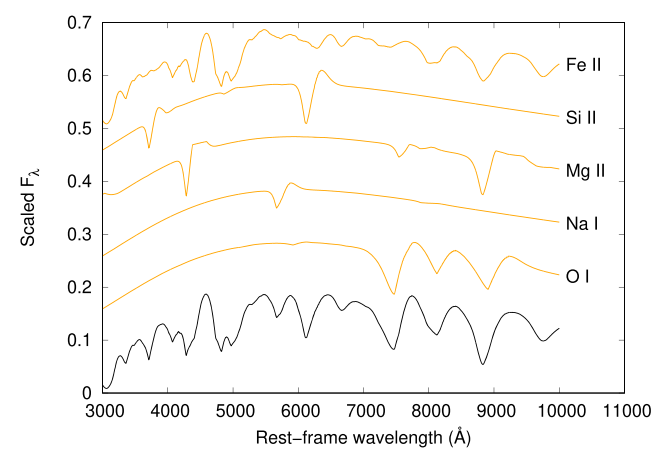


Figure 10. SYN++ modeling of the +29 days phase (2019 October 7) spectrum of SN 2019neq, with the same color coding as in Figure 6.

they are dominated by a hot blue continuum with some (weak) ionized carbon and oxygen features.

This remains true for the early post-maximum phases, even though the decrease in the continuum slope implies a cooling ejecta for both events. A significant difference between SN 2010kd and SN 2019neq is the characteristic timescale of their spectral evolution: the +5 days spectrum of SN 2019neq has a similar continuum slope to that of SN 2010kd at phase +14 days, again implying that SN 2019neq is a fast-evolving SLSN-I (see Figure 5).

The SYN++ models presented in Section 4 reveal that a weak C II feature may be present in the pre- and early post-maximum spectra of SN 2019neq. C II produced unambiguous, strong features in the -22 days spectrum of SN 2010kd, similar to other slowly evolving SLSNe-I (for example, SN 2015bn, Inserra et al. 2017; Yan et al. 2017, or SN 2018bsz, Anderson et al. 2018a, 2018b; Blanchard et al. 2018). The presence of weak C II in the spectra of SN 2019neq suggests that the outer ejecta of Fast SLSNe-I may also contain carbon, and thus they are similar to the ejecta of Slow SLSNe-I in this respect.

The top right panel of Figure 11 presents the evolution of the photospheric velocities as a function of the rest-frame phase since B-band maximum in the case of SN 2010kd and ZTF gband maximum in the case of SN 2019neq. It can be seen that the velocity of SN 2010kd is nearly constant over the observed epochs, implying that the outer ejecta remains optically thick up to ~+35 rest-frame days after maximum. On the other hand, SN 2019neq shows a factor of  $\sim$ 2 higher  $v_{\rm phot}$  around maximum light that quickly decreases to  $\sim$ 12,000 km s<sup>-1</sup> (a more typical  $v_{\text{phot}}$  value for SLSNe) by the +30 days phase. This fast decline in velocity is probably caused by the steep decrease in the density in the outer ejecta, which may suggest a different density profile and somewhat lower ejecta mass for SN 2019neq than for SN 2010kd. This is consistent with the results of the mass estimates presented in Section 5.3 below (see also Nicholl et al. 2015).

At *B*-band maximum, the photospheric velocities imply photospheric radii  $r_{\rm phot} \sim 6 \times 10^{15}\,{\rm cm}$  for SN 2010kd and  $r_{\rm phot} \sim 5 \times 10^{15}\,{\rm cm}$  for SN 2019neq. The similar value of  $r_{\rm phot}$  is due to the fact that the shorter rise time of SN 2019neq is compensated by its larger ejecta velocity.

In the bottom panels of Figure 11, the evolution of the optical depths of C II and Fe II are presented. The optical depth of C II is the same order of magnitude for SN 2010kd and

SN 2019neq, if present. Both objects show a swift fall-off in C II  $\log \tau$  after maximum; by the +30 days phase, the  $\log \tau$  value of SN 2010kd decreases to  $\sim$ -2, while C II flux is not detected in the case of SN 2019neq. This behavior is consistent with the observations of other SLSNe, where the carbon features can be found only before or around maximum, and they quickly diminish in post-maximum phases (e.g., Inserra et al. 2018; Quimby et al. 2018).

In contrast, the optical depth of Fe II differs between the two objects; it is nearly constant for SN 2010kd after maximum, while it rises rapidly for SN 2019neq over similar phases. This is related to the strengthening of the Fe II features with decreasing temperature, as seen, e.g., in the post-maximum spectra of SNe Ia during the "Fe II phase" (Branch & Wheeler 2017). We note here that the computed Fe II optical depth for the +29 days spectrum of SN 2019neq is based on only a single feature, thus it may be overestimated.

#### 5.3. Lower Limits to the Ejecta Mass

It is possible to give constraints on the ejecta mass from the criterion that the total optical depth  $(\tau_{\rm tot})$  for the inner, opaque ejecta should be  $\tau_{\rm tot} > 1$  during the photospheric phase. We can estimate  $\tau_{\rm tot} \sim \kappa \rho r_{\rm phot}$ , where  $r_{\rm phot}$  can be inferred from the expression of homologous expansion as  $r_{\rm phot} = v_{\rm phot}(t-t_0)/(1+z)$  (where  $t_0$  is the explosion date). We can then estimate the density as

$$\rho \sim \frac{\tau_{\text{tot}}}{\kappa r_{\text{phot}}}.$$
 (7)

The total optical depth below the photosphere around maximum,  $\tau_{\rm tot}$ , can be inferred from the formulae of Arnett (1996) (see also Branch & Wheeler 2017) as  $\tau_{\rm tot} \approx 3c/v_{\rm sc}$ , where  $v_{\rm sc}$  is the scaling velocity of the homologously expanding ejecta that we approximate with  $v_{\rm sc} = v_{\rm phot}$  at maximum light. We also assume that the total opacity,  $\kappa$ , inside the opaque SN ejecta can be approximated by the Thompson scattering opacity of an H-poor SN envelope,  $\kappa \sim 0.1 \, {\rm cm}^2 \, {\rm g}^{-1}$ .

After calculating the density from Equation (7), the total ejecta mass is estimated by assuming a constant density distribution and using the photospheric radius from the

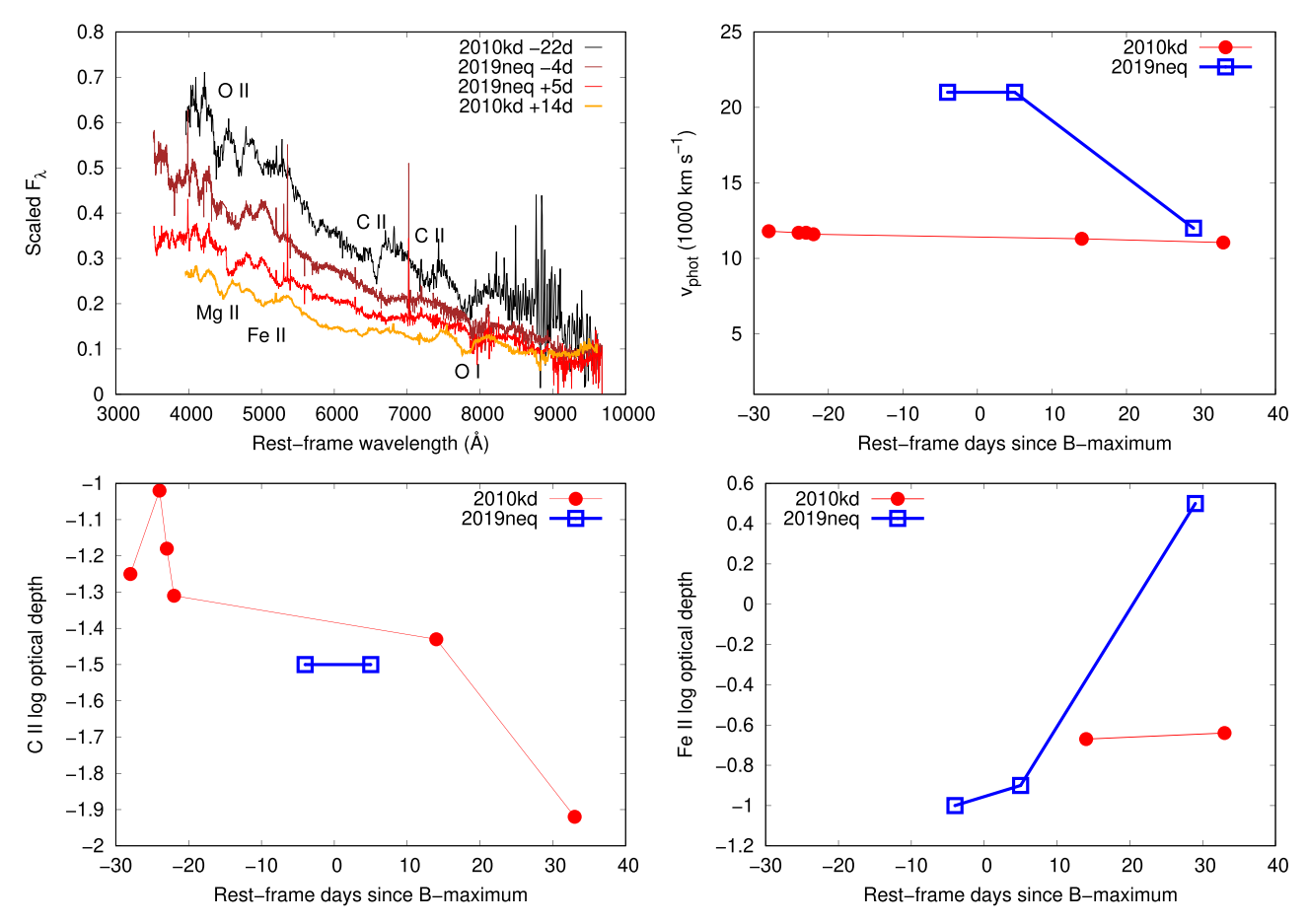


Figure 11. Comparison of the spectral evolution of SN 2019neq and SN 2010kd before and shortly after maximum light. Top left panel: spectra that have been Doppler-shifted back to zero photospheric velocity, showing the major identified features. Top right panel: photospheric velocity evolution. Bottom left panel: evolution of the optical depth of the C II reference line. Bottom right panel: the same as the bottom left panel but for the Fe II reference line.

homologous expansion:

$$M_{\rm ej} = \frac{4\pi}{3} r_{\rm phot}^3 \rho = \frac{4\pi}{3} \frac{v_{\rm phot}^2 (t - t_0)^2}{(1 + z)^2} \frac{\tau_{\rm tot}}{\kappa}.$$
 (8)

The predicted radius, ejecta mass, and optical depth values of SN 2019neq and SN 2010kd at maximum light are presented in Table 3. Our calculations show that the predicted mass limit for the Slow SLSN-I, SN 2010kd, ( $\sim$ 48  $M_{\odot}$ ) is more than a factor of 2 higher than the value belonging to the Fast SLSN-I, SN 2019neq ( $\sim$ 23  $M_{\odot}$ ). Since these are order-of-magnitude estimates, we cannot draw the conclusion that faster SLSNe-I possess less ejecta mass than slower SLSNe (Nicholl et al. 2015). In order to test this hypothesis we plan to examine a larger sample of SLSNe-I.

As a cross-check, we also compared our estimates of optical depth to the inferred  $\tau_{\rm tot}$  of a normal SN Ia at maximum, derived in the same way as above, using  $v_{\rm phot}=10,000\,{\rm km\,s^{-1}}$ ,  $(t-t_0)/(1+z)=18$  days, and  $M_{\rm ej}=1.44\,M_{\odot}$ . This gave  $\tau_{\rm tot}=28.42$ , which is roughly similar to the optical depths of the SLSNe-I listed in Table 3. This suggests that the masses given in Table 3 are valid order-of-magnitude estimates of the true ejecta masses.

Studying the nebular spectra of SLSNe can result in another constraint on the ejecta mass, since the whole atmosphere of the SN becomes transparent by this phase, revealing the innermost layers of the object. According to Maurer & Mazzali (2010),  $\sim$ 70% of the ejecta mass of Type Ib/c SNe consists of

 Table 3

 Estimates for the Ejecta Mass from the Total Optical Depth

SN	Days from Explosion	$r (10^{15} \text{cm})$	$ au_{ m tot}$	$M_{\rm ej}~(M_{\odot})$
SN 2010kd	52.5	6.1	60	48
SN 2019neq	31.0	5.1	43	23
SNe Ia	18.0	1.6	28	1.4

oxygen. The oxygen mass of SN 2010kd was recently published by Kumar et al. (2020) as  $\sim$ 20  $M_{\odot}$ . This is consistent with the mass derived from their bolometric light-curve modeling, and can be considered as a lower limit to the entire ejecta mass. Unfortunately, after having emerged from solar occlusion, the Fast SLSN-I SN 2019neq was too faint for nebular observations, and the spectra that we obtained did not contain sufficient signal for further analysis.

#### 6. Conclusions

We have presented a comparative spectral analysis of the recently discovered Fast SLSN-I SN 2019neq with the well-observed Slow SLSN-I SN 2010kd (Kumar et al. 2020) by modeling their photospheric-phase spectra.

The redshift- and extinction-corrected spectra of SN 2019neq at the three observed epochs (-4, +5, +29 days) were modeled using the SYN++ code (Thomas et al. 2011). The photospheric velocity in the first two spectra was roughly constant at  $21,000 \text{ km s}^{-1}$ , but steeply declined to  $12,000 \text{ km s}^{-1}$  by the

epoch of the third observation (+29 days), demonstrating a very fast velocity evolution. Over the same period, the photospheric temperature decreased from 15,000 to 12,000 K, then to 6000 K.

In the first spectrum of SN 2019neq (-4 days), we identified C II, C III, O III, Si III, Si IV, Co III, and Fe II lines. An alternative model containing O II instead of C III, O III, and Si IV was found to describe the W-shaped feature between 4300 and 4500 Å as well as the previous model.

This ambiguity is consistent with Hatano et al. (1999) and Dessart (2019), who demonstrated that around  $T \sim 15,000$  K the optical depths of the pairs of ionization states O II and O III, as well as C II and C III, are similar. The presence of C II (or C III) is somewhat unexpected, since ionized carbon was previously detected primarily in Slow SLSNe-I.

The second spectrum at +5 days contains similar elements and ionization states to the previous epoch, together with newly appearing C I lines. While a photospheric velocity of  $v_{\rm phot}=16,000~{\rm km\,s^{-1}}$  is suggested from the apparent position of the Fe II minimum (assuming that the feature corresponds exclusively to the Fe II  $\lambda 5169$  line), we found that the wavelength region  $4000-5000~{\rm \AA}$  is dominated by the blending of numerous weak Fe II lines, and that the observed feature minimum is unlikely to correspond to the line of Fe II  $\lambda 5169$ . After full spectral modeling with SYN++, we found that a model with  $v_{\rm phot}=21,000~{\rm km\,s^{-1}}$  more accurately fits the observed features.

The spectrum of the third epoch differs from the previous spectra regarding both the ion composition and the photospheric velocity. Since the photospheric temperature decreased to 6000 K, the neutral and low-ionized elements began to dominate over the lines of the highly ionized transitions that were present in the earlier spectra. At this epoch we identified O I, Na I, Mg II, Si II, and Fe II.

From the available spectra, it was possible to classify SN 2019neq by comparing its +29 days phase spectrum to the +85 days spectrum of the Slow SLSN-I SN 2010kd. Since the two spectra are similar, we concluded that SN 2019neq belongs to the class of Fast SLSNe-I, as determined by its spectroscopic characteristics. This is consistent with the estimated velocity gradient of  $\dot{v} \sim 375 \, \mathrm{km \, s^{-1}} \, \mathrm{day^{-1}}$  (inferred from SYN++ models), which is among the highest velocity gradients ever observed for SLSNe-I. Using the same methodology as Inserra et al. (2018) to measure the velocity gradient, we get  $\dot{v} \sim 100 \, \mathrm{km \, s^{-1}} \, \mathrm{day^{-1}}$ , which is similar to the velocity gradient observed for other Fast SLSNe-I (Inserra et al. 2018).

Using the optical depths of the reference features for each ion from our SYN++ models, we inferred the local densities of

each ion at the three observational epochs, and thereby revealed clues to the chemical composition of the object.

Our comparison of the evolution of the photospheric velocity and the optical depths of strong features (C II and Fe II in particular) of SN 2019neq with those of SN 2010kd suggested somewhat different ejecta parameters, such as the density profile and the total mass.

We also estimated the total ejecta mass from our calculations of optical depth around maximum light (Branch & Wheeler 2017), and found  $M_{\rm ej} \sim 23$  and  $\sim \! 48\,M_\odot$  for SN 2019neq and SN 2010kd respectively. These are consistent with the mass estimates from light-curve modeling of SLSNe-I (20–40  $M_\odot$ ) given by Chatzopoulos et al. (2013) and Nicholl et al. (2016), and exceed the typical SN Ia ejecta mass by at least one order of magnitude. We found a possible correlation between the ejecta mass and evolutionary timescale of SLSNe-I: faster evolving SLSNe may have lower ejecta masses. Since this statement is based on a small sample of objects, testing the reliability of this hypothesis requires many more SLSNe-I to be modeled using similar methods to those described above.

R.K.T. and J.V. are supported by the project "Transient Astrophysical Objects' GINOP 2.3.2-15-2016-00033 of the National Research, Development and Innovation Office (NKFIH), Hungary, funded by the European Union. R.K.T. is also supported by the UNKP-19-02 New National Excellence Program of the Ministry for Innovation and Technology. B.P.T. and J.C.W. are supported in part by NSF grant 1813825. This study is based on observations obtained with the Hobby-Eberly Telescope, which is a joint project of the University of Texas at Austin, the Pennsylvania State University, Ludwig-Maximilians-Universität München, and Georg-August-Universität Göttingen. The HET is named in honor of its principal benefactors, William P. Hobby and Robert E. Eberly. The Low Resolution Spectrograph 2 (LRS2) was developed and funded by the University of Texas at Austin McDonald Observatory and Department of Astronomy and by Pennsylvania State University. We thank the Leibniz-Institut für Astrophysik Potsdam (AIP) and the Institut für Astrophysik Göttingen (IAG) for their contributions to the construction of the integral field units.

#### **Appendix**

Tables A1, A2, and A3 summarize the modeled and calculated parameters of SN 2019neq.

 Table A1

 Best-fit Local Parameters of the SYN++ Photospheric-phase Models of SN 2019neq

Element	$\log  au$	$(10^3  \text{km s}^{-1})$	$(10^3  \text{km s}^{-1})$	$\sigma (10^3 \text{ km s}^{-1})$	$T_{\rm exc} (10^3 { m K})$
MJD 58727 (-4)					
Сп	-1.2	21.0	50.0	5.0	15.0
C III	-0.2	21.0	50.0	2.0	30.0
O III	1.0	21.0	50.0	1.0	15.0
Si III	0.2	21.0	50.0	2.0	20.0
Si IV	0.0	21.0	50.0	2.0	20.0
Fe II	-1.0	21.0	50.0	2.0	15.0
Co III	-0.5	21.0	50.0	2.0	20.0
MJD 58727 (-4) Alternative model					
Сп	-1.5	21.0	50.0	1.0	15.0
ОП	-1.7	21.0	50.0	1.0	15.0
Si III	0.0	21.0	50.0	2.0	20.0
Fe II	-1.0	21.0	50.0	1.0	15.0
Co III	-0.5	21.0	50.0	2.0	20.0
MJD 58737 (+5)					_
CI	0.0	21.0	50.0	2.0	12.0
Сп	-1.5	21.0	50.0	5.0	12.0
O III	0.7	21.0	50.0	1.0	12.0
Si III	0.2	21.0	50.0	2.0	12.0
Si IV	-0.3	21.0	50.0	2.0	12.0
Fe II	-0.9	21.0	50.0	2.0	12.0
Co III	-0.5	21.0	50.0	2.0	18.0
MJD 58763 (+29)					
01	0.0	12.0	50.0	5.0	6.0
Na I	-0.2	12.0	50.0	2.0	6.0
Mg II	0.7	12.0	50.0	2.0	6,0
Si II	0.3	12.0	50.0	2.0	6.0
Fe II	0.5	12.0	50.0	2.0	11.0

 Table A2

 Parameters Required to Compute the Number Density of Individual Species of SN 2019neq for Each Epoch

Element	$\log \tau$	g	$\log(gf)$	T (K)	λ (Å )	$t_d$ (days)	z(T)	χ (eV)
MJD 58727 (-4)								
Сп	-1.2	6	0.77	15000	4267	24.4	6.18	18.07
CIII	-0.2	3	0.08	30000	4647	24.4	1.77	29.57
Si III	0.2	5	0.18	15000	4553	24.4	1.06	19.04
Si IV	0.0	2	0.20	20000	4089	24.4	2.03	24.08
Fe II	-1.0	10	-1.40	15000	5018	24.4	100.64	2.89
Co III	-1.0	8	-2.36	20000	4433	24.4	46.64	10.41
MJD 58727 (-4) Alternative								
Сп	-1.5	6	0.77	15000	4267	24.4	6.18	18.07
Si III	0.00	5	0.18	20000	4553	24.4	1.21	19.04
Fe II	-1.0	10	-1.40	15000	5018	24.4	100.64	2.89
Co III	-0.5	8	-2.36	20000	4433	24.4	46.64	10.41
MJD 58737 (+5)								
CI	0.0	5	0.07	12000	9095	33.5	10.69	7.49
CII	-1.5	6	0.77	12000	4267	33.5	6.04	18.07
Si III	0.2	5	0.18	12000	4553	33.5	1.02	19.04
Si IV	-0.3	2	0.20	12000	4089	33.5	2.00	24.08
Fe II	-0.9	10	-1.40	16000	5018	33.5	108.78	2.89
Co III	-0.5	8	-2.36	18000	4433	33.5	42.81	10.41
MJD 58763 (+29)								
10	0.00	5	0.32	6000	7772	57	8.95	9.16
Na I	-0.2	2	0.12	6000	5890	57	2.19	0.00
Mg II	0.7	4	0.74	6000	5184	57	2.00	8.87
Si II	0.3	2	0.30	6000	6347	57	5.73	8.13
Fe II	0.5	6	-1.4	11000	5018	57	72.75	2.89

Table A3
Inferred Values of the Number and Mass Densities of Each Ionization State in SN 2019neq at All Epochs

Element	$\frac{\log n_l}{(\text{cm}^{-3})}$	$\log N$ (cm <sup>-3</sup> )	Mass Number	$\log \rho$ (g cm <sup>-3</sup> )
MJD 58727				
(-4 days)				
CII	3.02	5.67	12	-17.03
C III	4.71	6.64	12	-16.06
Si III	4.93	7.04	28	-15.29
Si IV	4.44	7.08	28	-15.25
Fe II	5.62	7.04	56	-14.99
Co III	6.60	8.51	59	-13.50
MJD 58727 (-4) Alternative				
Сп	2.72	5.37	12	-17.33
Si III	4.86	6.33	28	-16.01
Fe II	7.10	9.01	56	-13.02
Co III	5.62	7.04	59	-14.97
MJD 58737 (+5)				
Cı	4.61	6.31	12	-16.39
CII	2.49	5.79	12	-16.91
Si III	4.70	7.48	28	-14.85
Si IV	3.78	8.17	28	-14.16
Fe II	5.61	7.04	56	-14.99
Co III	6.92	8.91	59	-13.09
MJD 58763 (+29)				
01	3.83	7.42	16	-15.15
Na I	3.43	3.47	22	-18.97
Mg II	4.01	6.95	24	-15.45
Si II	3.75	7.17	28	-15.16
Fe II	6.39	8.05	56	-13.98

### **ORCID** iDs

Réka Könyves-Tóth https://orcid.org/0000-0002-8770-6764

Benjamin P. Thomas https://orcid.org/0000-0002-0977-1974

József Vinkó https://orcid.org/0000-0001-8764-7832 J. Craig Wheeler https://orcid.org/0000-0003-1349-6538

#### References

Anderson, J. P., Dessart, L., Pessi, P., et al. 2018a, ATel, 11674, 1 Anderson, J. P., Pessi, P. J., Dessart, L., et al. 2018b, A&A, 620, A67

```
Angus, C. R., Levan, A. J., Perley, D. A., et al. 2016, MNRAS, 458, 84
Angus, C. R., Smith, M., Sullivan, M., et al. 2019, MNRAS, 487, 2215
Arnett, D. 1996, Supernovae and Nucleosynthesis: An Investigation of the
  History of Matter (Princeton, NJ: Princeton Univ. Press)
Barbon, R., Buondi, V., Cappellaro, E., et al. 2008, yCat, 2, 283
Bellm, E. C., Kulkarni, S. R., Graham, M. J., et al. 2019, PASP, 131,
  018002
Blanchard, P., Nicholl, M., Chornock, R., et al. 2018, ATel, 11790, 1
Branch, D., & Wheeler, J. C. 2017, Supernova Explosions: Astronomy and
  Astrophysics Library (Berlin: Springer)
Brown, P. J., Breeveld, A. A., Holland, S., et al. 2014, Ap&SS, 354, 89
Chatzopoulos, E., Wheeler, J. C., Vinko, J., et al. 2013, ApJ, 773, 76
Chen, T.-W., Schady, P., Xiao, L., et al. 2017, ApJL, 849, L4
Chonis, T. S., Hill, G. J., Lee, H., et al. 2016, Proc. SPIE, 9908, 99084C
De Cia, A., Gal-Yam, A., Rubin, A., et al. 2018, ApJ, 860, 100
de Jaeger, T., Zheng, W., Stahl, B. E., et al. 2019, MNRAS, 490, 2799
Dessart, L. 2019, A&A, 621, A141
Fisher, P. 2000, PhD thesis, Univ. Oklahoma
Gal-Yam, A. 2012, Sci, 337, 927
Hatano, K., Branch, D., Fisher, A., et al. 1999, ApJS, 121, 233
Inserra, C. 2019, NatAs, 3, 697
Inserra, C., Nicholl, M., Chen, T.-W., et al. 2017, MNRAS, 468, 4642
Inserra, C., Prajs, S., Gutierrez, C. P., et al. 2018, ApJ, 854, 175
Inserra, C., Smartt, S. J., Jerkstrand, A., et al. 2013, ApJ, 770, 128
Jha, S. W., Maguire, K., & Sullivan, M. 2019, NatAs, 3, 706
Kumar, A., Pandey, S. B., Konyves-Toth, R., et al. 2020, ApJ, 892, 28
Leloudas, G., Schulze, S., Krühler, T., et al. 2015, MNRAS, 449, 917
Lennarz, D., Altmann, D., & Wiebusch, C. 2012, A&A, 538, A120
Liu, Y.-Q., Modjaz, M., & Bianco, F. B. 2017, ApJ, 845, 85
Lunnan, R., Chornock, R., Berger, E., et al. 2013, ApJ, 771, 97
Lunnan, R., Chornock, R., Berger, E., et al. 2014, ApJ, 787, 138
Lunnan, R., Chornock, R., Berger, E., et al. 2018, ApJ, 852, 81
Maurer, I., & Mazzali, P. A. 2010, MNRAS, 408, 947
Mazzali, P. A., Sullivan, M., Pian, E., et al. 2016, MNRAS, 458, 3455
Modjaz, M., Liu, Y. Q., Bianco, F. B., et al. 2016, ApJ, 832, 108
Mulligan, B. W., Zhang, K., & Wheeler, J. C. 2019, MNRAS, 484,
Nicholl, M., Berger, E., Smartt, S. J., et al. 2016, ApJ, 826, 39
Nicholl, M., Blanchard, P. K., Berger, E., et al. 2018, ApJL, 866, L24
Nicholl, M., Smartt, S. J., Jerkstrand, A., et al. 2015, MNRAS, 452, 3869
Nordin, J., Brinnel, V., Giomi, M., et al. 2019, Transient Name Server
  Discovery Report 2019-1472, 1
Pastorello, A., Smartt, S. J., Botticella, M. T., et al. 2010, ApJL, 724, L16
Perley, D. A., Quimby, R. M., Yan, L., et al. 2016, ApJ, 830, 13
Perley, D. A., Yan, L., Gal-Yam, A., et al. 2019, TNSAN, 79, 1
Quimby, R. M. 2006, PhD thesis, Univ. Texas Austin
Quimby, R. M., Aldering, G., Wheeler, J. C., et al. 2007, ApJL, 668, L99
Quimby, R. M., De Cia, A., Gal-Yam, A., et al. 2018, ApJ, 855, 2
Schlafly, E. F., & Finkbeiner, D. P. 2011, ApJ, 737, 103
Schulze, S., Krühler, T., Leloudas, G., et al. 2018, MNRAS, 473, 1258
Silverman, J. M., Vinkó, J., Marion, G. H., et al. 2015, MNRAS, 451,
Smith, K. W., Williams, R. D., Young, D. R., et al. 2019, RNAAS, 3, 26
Smith, N., Li, W., Foley, R. J., et al. 2007, ApJ, 666, 1116
Thomas, B. P., Konyves-Toth, R., Vinko, J., et al. 2019, ATel, 13184, 1
Thomas, R. C., Nugent, P. E., & Meza, J. C. 2011, PASP, 123, 237
Vinko, J., Zheng, W., Romadan, A., et al. 2010, CBET, 2556, 1
Yan, L., Lunnan, R., Perley, D. A., et al. 2017, ApJ, 848, 6
```

Yan, L., Quimby, R., Ofek, E., et al. 2015, ApJ, 814, 108